remote sensing

MDPI

Article

Impact of Plasma Bubbles on OTHR Shortwave Propagation in Different Backgrounds

Xin Ma [1], Peng Guo [1], Ding Yang [2,*], Mengjie Wu [1] and Hengyi Yue [1]

[1] Shanghai Astronomical Observatory, Chinese Academy of Sciences, Shanghai 200030, China; maxinee@foxmail.com (X.M.)
[2] Communication Engineering School, Hangzhou Dianzi University, Hangzhou 310005, China
* Correspondence: yangding@hdu.edu.cn

Abstract: Plasma bubbles represent notable ionospheric irregularities primarily observed in low latitudes, characterized by plasma depletions exhibiting large spatial scales, which can make a significant impact on the propagation of OTHR (over-the-horizon radar) waves. Firstly, we constructed a three-dimensional model of plasma bubbles, which is modulated by Gaussian function distribution in the horizontal direction, and then we analyzed the impact of EPBs (Equatorial Plasma Bubbles) on the ray path of OTHR shortwaves. When radio waves propagate through EPBs with different RMS $\Delta N/N$, there is a significant difference in the propagation path of OTHR waves. For the EPB with an RMS $\Delta N/N$ of 75%, radio waves exhibit more pronounced refraction than those with lower RMS values, the focusing effect of radio waves is more obvious, and the focusing point is relatively lower. In terms of different seasons, OTHR shortwaves propagating through EPBs exhibit different degrees of refraction. In addition, radio waves show the effect of inward focusing in different seasons: the focusing effect is the most pronounced in spring, followed by autumn, then summer, and the weakest in winter. For different solar activities, the impact of EPBs on OTHR shortwaves is more significant in the high-solar-activity year.

Keywords: plasma bubbles; OTHR shortwaves; three-dimensional model; focusing effect

Citation: Ma, X.; Guo, P.; Yang, D.; Wu, M.; Yue, H. Impact of Plasma Bubbles on OTHR Shortwave Propagation in Different Backgrounds. *Remote Sens.* **2024**, *16*, 2494. https://doi.org/10.3390/rs16132494

Academic Editor: Jonathan H. Jiang

Received: 8 May 2024
Revised: 28 June 2024
Accepted: 3 July 2024
Published: 8 July 2024

1. Introduction

The ionospheric irregularities associated with plasma instability after sunset are collectively known as Equatorial Spread F (ESF). Initially proposed by Booker and Wells [1], ESF refers to diffuse extended structures observed in the F-layer trace on ionograms. Well-developed ESF structures are termed Equatorial Plasma Bubbles (EPBs), and Rayleigh–Taylor instability [2,3] plays an important role in the formation of EPBs after sunset. EPBs typically have a horizontal width of several hundred kilometers [4,5] and extend along magnetic field lines to the latitudes of about 20° [6]. These ionospheric irregularities in the F region often appear as bubble-like or feather-like structures [7], and dark band can be observed in optical images from All-Sky airglow Imagers [8,9]. The presence of ionospheric F-layer irregularities has a significant effect on sky-wave propagation and high-frequency (HF) communications [10]. OTHR (over-the-horizon radar) can achieve the purpose of detecting long-range targets through the working principle, which corresponds to the refraction and backscattering effect of radar electromagnetic waves by the ionosphere [11,12]. When OTHR waves encounter irregularities in the ionosphere, fluctuations in the electron concentration will interfere with radio wave transmission. Ionospheric irregularities can generally reduce the operation frequency of sky-wave radar, affect the accurate positioning of long-range detection targets, and cause an increase in positioning errors.

To simulate radar wave propagation through the ionosphere, three-dimensional (3D) ray tracing is an effective tool. Han et al. [13] reported an electron concentration model for the Es layer and conducted a simulation analysis of its effects on sky-wave radar via 3D

ray-tracing technology. Carrano et al. [14] developed the Radio Occultation Scintillation Simulator (ROSS), which adopts a Multi-Phase Screen (MPS) to simulate the forward scattering of radio waves caused by ionospheric irregularities. Thayaparan et al. [15] reported patches with enhanced electron density in the polar ionosphere and utilized numerical ray tracing to analyze the impact of the structures on the propagation path of OTHR waves, which can be applied in the OTHR frequency monitoring system. Using a ray-tracing method, Zhao et al. [16] investigated the multipath effect of radio wave propagation through the artificial plasma cloud [17], which is caused by the release of cesium (Cs) vapor in the upper atmosphere, and obtained the coherent bandwidth of the spatial channel. Ma et al. [18] simulated the electron density cavity generated by the release of rocket plume chemicals and investigated its effects on OTHR shortwaves at different frequencies using a 3D ray-tracing algorithm.

The ionospheric irregularities generally include EPBs, sporadic E (Es), equatorial ionization anomaly (EIA), etc. [2,5,19]. At present, regarding the impact of ionospheric irregularities on OTHR, research has been conducted on the influence of ionospheric Es irregularities on sky-wave radar [13,20]. However, studies on the impact of F-layer irregularities on OTHR are scarce. Therefore, this study aims to establish a three-dimensional electron density model of plasma bubbles and simulate the ray paths of HF waves propagating through EPBs. Based on a 3D ray-tracing algorithm, we will analyze and evaluate the influence of F-layer irregularities on OTHR radio waves at different frequencies. This study can provide technical support for OTHR and effectively improve the detection performance of sky-wave radar.

2. Modeling and Methods

2.1. Modeling and Simulation of Plasma Bubbles

In this study, we refer to a simple model of plasma bubbles proposed by Carrano [14], which is modulated by the Gaussian distribution function in the east–west orientation. For the three-dimensional modeling of plasma bubbles, it is reasonable to assume that (1) there is nearly no variation in the electron concentration toward the north–south direction, and (2) electron density fluctuations are approximately isotropic. The geometric diagram for plasma bubble modeling is illustrated in Figure 1.

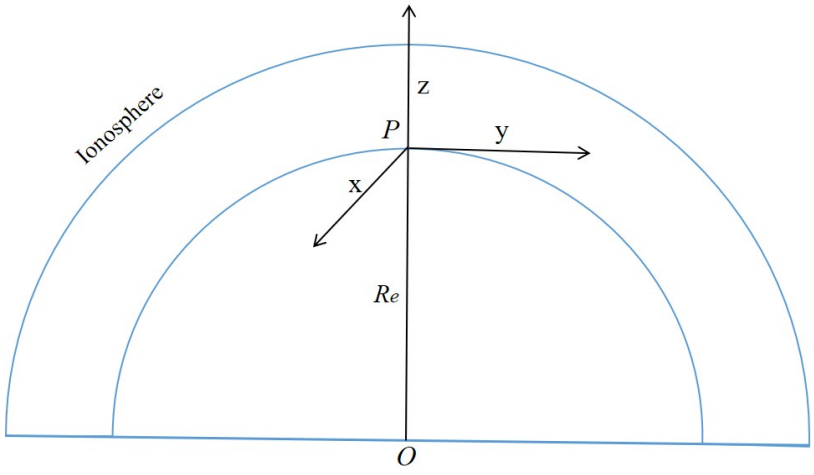

Figure 1. Geometric coordinate diagram of EPB.

In Figure 1, point O represents the center of the earth, point P represents the origin of the coordinate system corresponding to the site of the ground transmitter, and *Re* is the average radius of the earth. The x-axis points to the south along the magnetic field, the y-axis points to the east, and the z-axis points vertically upward from the ground.

Due to the uniform electron concentration toward the north–south orientation, we mainly focused on the density fluctuations of the EPB in the plane of the *y*- and *z*-axes. In

the EPB simulation, $N_B(\mathrm{y},\mathrm{z})$ stands for the electron density of the ionospheric background, which can be obtained through the IRI-2016 model. It is assumed that the RMS of $\Delta N/N$ (electron density fluctuations) is a constant along the z-axis orientation independent of height, as shown in Formula (1).

$$\sigma(\Delta N/N) = RMS(\frac{\Delta N(\mathrm{y},\mathrm{z})}{N(\mathrm{y},\mathrm{z})}) = const \tag{1}$$

Then, we simulated a Gaussian bubble with random fluctuations in the east–west direction. Formula (2) is a Gaussian distribution function, which is modulated with the Earth-centered angle as the parameter.

$$B(\mathrm{y},\mathrm{z}) = \exp\left\{-[\alpha(\mathrm{y},\mathrm{z}) - \alpha_0]^2/(2{\sigma_\alpha}^2)\right\} \tag{2}$$

In Formula (2), $\alpha(\mathrm{y},\mathrm{z}) = \tan^{-1}[\mathrm{y}/(\mathrm{z}+R_e)]$ and represents the Earth-centered angle. α_0 is the Earth-centered angle at the EPB center, $\alpha_0 = \tan^{-1}[\mathrm{y}_0/(hmF2 + R_e)]$, $hmF2$ stands for the peak altitude of the ionospheric F2 region, and it is assumed that the EPB appears at the altitude of $hmF2$. The standard deviation [14] in Formula (2) is presented as follows, which can be related to the EPB scale in the east–west orientation, L_H.

$$\sigma_\alpha = L_H/(\mathrm{A}(hmF2 + R_e)) \tag{3}$$

From the above formula, A refers to a scaling factor; here, the A value is specified as 1.348 based on Carrano's EPB model.

$$N(\mathrm{y},\mathrm{z}) = N_B(\mathrm{y},\mathrm{z})[1 - \sigma_{\Delta N/N} B(\mathrm{y},\mathrm{z})] \tag{4}$$

Finally, the total density field can be obtained by adding the density fluctuations to the background ionosphere, as shown in Formula (4). The EPB model is modulated by the Gaussian function in the east–west direction. This approach accounts for the local density fluctuations within the EPB, which vary with horizontal distance but remain constant with altitude.

2.2. Three-Dimensional Ray-Tracing Algorithm

Three-dimensional (3D) ray tracing can be an effective means for studying radio wave propagation, accurately reflecting the propagation path of radar waves in the ionosphere. The 3D ray-tracing method [21] is used to determine the reflection height of high-frequency (HF) waves and calculate the energy loss based on the ray path. Numerical ray tracing can be applied to the non-uniform ionosphere, and the code is easy to implement, making it widely used in the field of radio wave propagation.

Combined with the Appleton–Hartree formula, 3D numerical ray tracing employs the Runge–Kutta method to solve the Haselgrove differential equation, which is derived from Fermat's principle. The numerical solution of the Haselgrove equation is considered one of the most effective means of ionospheric ray tracing, enabling users to estimate the propagation path of transmitted rays from a certain point in other directions. Since the frequency of emitted electromagnetic waves is relatively high, the influence of the geomagnetic field can be ignored when considering the reflection of radio waves. Figure 2 illustrates the spherical coordinate system used in 3D ray tracing.

In Figure 2, OXYZ forms a Cartesian rectangular coordinate system, with the origin O at the center of the Earth, and OXY represents the equatorial plane. $\vec{k} = (k_r, k_\varphi, k_\theta)$, and it is the wave vector at point Q, where k_φ points toward the geographic east direction, k_θ is directed southward, and k_r is directed vertically upward from the ground.

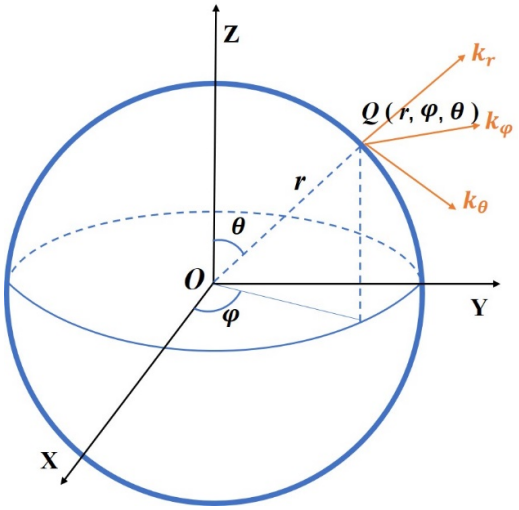

Figure 2. Spatial coordinate diagram of 3D ray tracing.

Based on the coordinate system above, the Haselgrove equations are presented below.

$$\begin{cases} \frac{dr}{dP'} = \frac{c}{\omega}k_r \\ \frac{d\theta}{dP'} = \frac{c}{\omega r}k_\theta \\ \frac{d\varphi}{dP'} = \frac{c}{r\omega\sin\theta}k_\varphi \\ \frac{dk_r}{dP'} = -\frac{\omega}{2c}\frac{\partial X}{\partial r} + {k_\theta}^2\frac{c}{r\omega} + {k_\varphi}^2\frac{c}{r\omega} \\ \frac{dk_\theta}{dP'} = \frac{1}{r}\left(-\frac{\omega}{2c}\frac{\partial X}{\partial \theta} - k_r k_\theta\frac{c}{\omega} + {k_\varphi}^2\frac{c}{\omega}\cot\theta\right) \\ \frac{dk_\varphi}{dP'} = \frac{1}{r\sin\theta}\left(-\frac{\omega}{2c}\frac{\partial X}{\partial \varphi} - k_\theta k_r\frac{c}{\omega}\sin\theta + \frac{c}{\omega}k_\theta k_\varphi\cos\theta\right) \end{cases} \quad (5)$$

In Equation (5), P' represents the group path, c denotes the light speed, $\omega = 2\pi f$, and f is the transmitted wave frequency. $X = {\omega_{pe}}^2/\omega^2$, and ω_{pe} is the angular frequency of the plasma. It should be noted that the Appleton–Hartree formula is simplified in this equation, and the refractive index is $n = \sqrt{1 - X}$.

In the actual simulation, a fast algorithm is adopted to perform shortwave ray tracing, and the group path step size is adaptively adjusted based on the gradient of X.

$$dP' = \frac{pX}{\frac{\partial X}{\partial r} + \frac{\partial X}{\partial \varphi} + \frac{\partial X}{\partial \theta}} \quad (6)$$

In Equation (6), p stands for the empirical coefficient, and it is often taken as 0.01. In addition, the Richard extrapolation method can be used to calculate the partial derivative of X, and the method for calculating the partial derivative is shown in Formula (7).

$$\begin{aligned} \frac{\partial X}{\partial r} &\approx \frac{4}{3}\frac{X(r+h/2,\theta,\varphi) - X(r-h/2,\theta,\varphi)}{h} - \frac{1}{6}\frac{X(r+h,\theta,\varphi) - X(r-h,\theta,\varphi)}{h} \\ \frac{\partial X}{\partial \theta} &\approx \frac{4}{3}\frac{X(r,\theta+h/2,\varphi) - X(r,\theta-h/2,\varphi)}{h} - \frac{1}{6}\frac{X(r,\theta+h,\varphi) - X(r,\theta-h,\varphi)}{h} \\ \frac{\partial X}{\partial \varphi} &\approx \frac{4}{3}\frac{X(r,\theta,\varphi+h/2) - X(r,\theta,\varphi-h/2)}{h} - \frac{1}{6}\frac{X(r,\theta,\varphi+h) - X(r,\theta,\varphi-h)}{h} \end{aligned} \quad (7)$$

3. Three-Dimensional Simulation Results of EPB

Based on the ionospheric irregularity model, we constructed a preliminary and simple EPB model in this study, which incorporates non-uniform random fluctuations with external scales, using the IRI-2016 model as the background ionosphere. According to our previous research work on EPB simulation [10], here, we simulated an ellipsoidal-shaped plasma bubble and added Gaussian distributed random fluctuations in the horizontal

orientation. Optical observations show that the scale of the plasma bubble in the north–south orientation is larger than in the east–west orientation [22], so the spatial scales were correspondingly set as 200 and 100 km in the two directions, and the spatial scale in the height direction was set to 60 km [14,23]. The electron density within the plasma bubble is markedly lower than that of the surrounding ionosphere, typically decreasing by tens of percent to three orders of magnitude [24]. For the EPB simulation, we assume that the RMS $\Delta N/N$ is 35% at the center of the EPB, and the EPB appears at an altitude of *hmF*2 (276 km). The simulation location was set in the Haikou region, located in Hainan, China, with a latitude and longitude of 20° N and 110° E, and the time was set to 20 LT at night on 15 September 2019. The east–west scale of the simulated EPB was set to 100 km. Figure 3 illustrates the three-dimensional electron density profile of the plasma bubble.

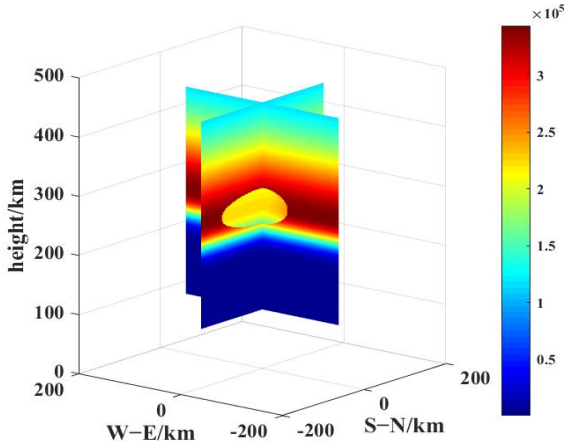

Figure 3. Three-dimensional electron density profile of the EPB.

From Figure 3, it can be observed that there is a region of electron density depletion at the height of the ionospheric F-layer. The simulated plasma bubble displays an ellipsoidal electron concentration hole, characterized by significantly lower electron density compared to the ionospheric background. In the three-dimensional coordinate system, the plasma bubble is centered at (0, 0, 276 km), with its spatial scale being notably larger in the north–south direction compared to the east–west direction. For the EPB simulation, there is negligible electron concentration variation in the north–south direction, and the electron density fluctuations conform to the Gaussian function distribution in the east–west direction.

The profiles of the plasma bubble in the east–west and north–south directions are shown in the figure below. Figure 4a,b illustrate the electron density slices at x = 0 and y = 0 in Figure 3, and the center of the plasma bubble is located at *hmF*2 height. From Figure 4, the plasma bubble shows an elliptical shape in the north–south and east–west orientations, with spatial scales of 200 km and 100 km, respectively. The scale of the plasma bubble in the north–south orientation is notably larger than that in the east–west orientation. From Figure 4a, there is the largest decrease in electron density at the center of the EPB, and the density fluctuations gradually decrease toward both sides, while the electron density of the EPB is uniform and unchanged in the north–south direction, as shown in Figure 4b.

Figure 5 shows the electron concentration profiles of the ionospheric IRI and EPB, and the EPB profile corresponds to the electron density profile at x = 0 and y = 0 in Figure 3. As can be seen from Figure 5, there is a significant electron density depletion in the F-layer of the ionosphere. Within the height range corresponding to the EPB, the electron density is notably lower compared to the IRI model. At the *hmF*2 altitude of the ionosphere, the decrease in electron density reaches its maximum. Observations indicate that EPBs usually exhibit feather-like morphology, and EPB structures may be embedded with irregularities of various scales. Compared to the background ionosphere, the electron density inside the EPB may decrease by 2–3 orders of magnitude. Considering the morphology and density gradient of EPBs, there are some differences between the present model and real EPBs. In

this study, we mainly conducted a preliminary simulation of an EPB and then analyzed its effects on OTHR radio wave propagation.

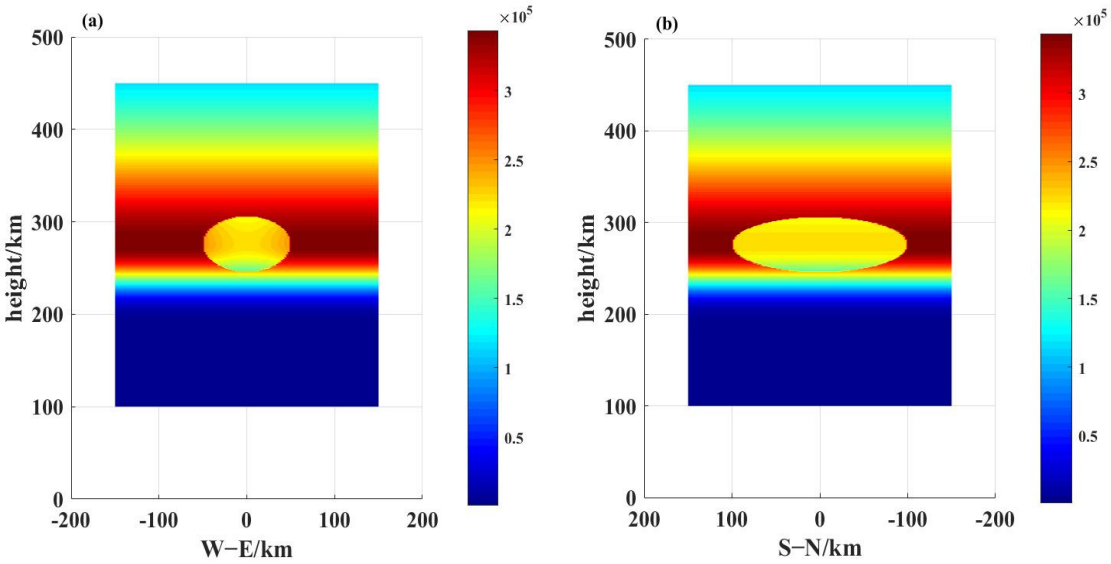

Figure 4. EPB profile in two directions. (**a**) EPB profile in the east−west direction; (**b**) EPB profile in the north−south direction.

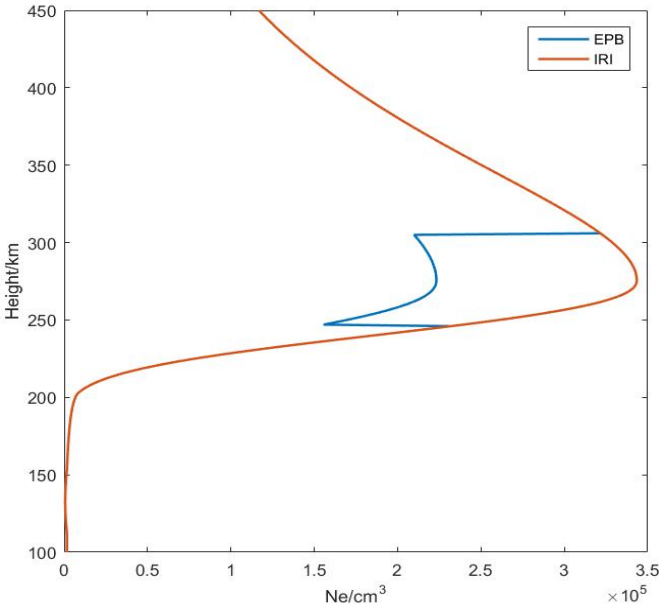

Figure 5. Electron density profile of IRI and EPB.

4. Simulation Results of OTHR Radio Waves Propagating through EPBs

4.1. Simulation Results of OTHR Radio Waves for Different EPBs

Based on the established model of an EPB, the echo path of OTHR shortwaves through EPBs was simulated. For EPBs with different RMS $\Delta N/N$, their effects on the propagation path of OTHR waves were analyzed and investigated. The RMS $\Delta N/N$ at the center of the EPBs was set to 35% and 75%, respectively, and labeled as P1 and P2. In this simulation, the time was set to 20 LT on 15 September 2019, and the location was set in the Haikou area. The transmission frequency of OTHR waves was 6, 8, and 10 MHz, and the elevation angle ranged from 75° to 105°. The shortwaves were transmitted by default toward the east, with an azimuth angle of 90°, and the interval angle of each ray was 2°. Figure 6 presents the

simulation results of 6 MHz shortwaves propagating through the EPBs, and the electron density background represents the slice of the plasma bubbles in the east–west orientation.

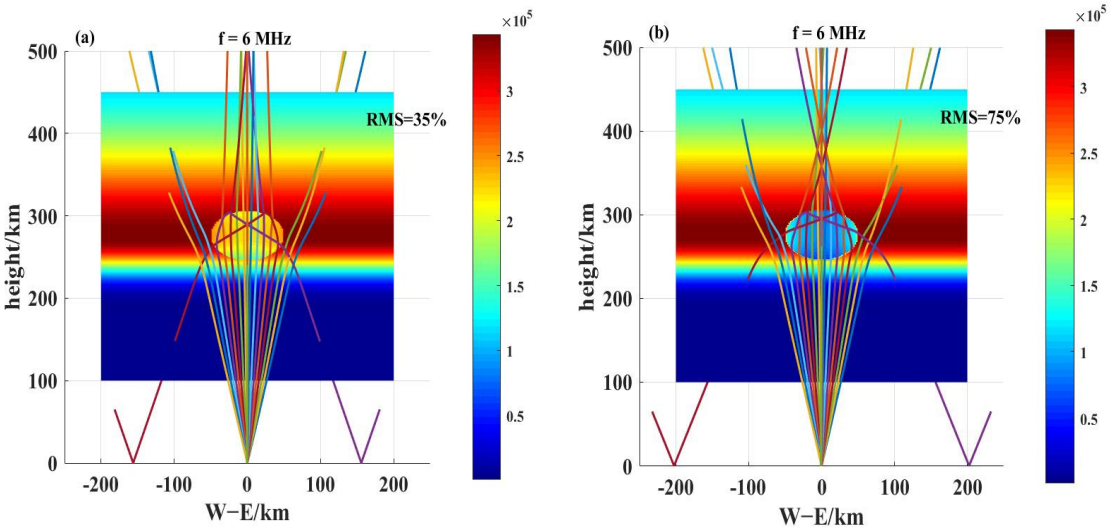

Figure 6. Simulation results of 6 MHz shortwaves propagating through EPBs. (**a**) Simulation results of 6 MHz waves propagating through EPB with RMS=35%; (**b**) Simulation results of 6 MHz waves propagating through EPB with RMS = 75%.

In Figure 6, the frequency of the transmitted shortwaves is 6 MHz, and radio waves produce a pronounced refraction effect when passing through the EPB, displaying distinct features of inward focusing. Some of the radio rays are reflected to the ground, while the majority penetrate the EPB and continue to propagate upward. In general, radio waves show a phenomenon of partial penetration and partial reflection. Specifically, radio rays with lower elevation will undergo reflection at the upper boundary of the plasma bubble, subsequently returning to the ground.

When OTHR shortwaves propagate through EPBs with different RMS, their echo paths are completely different. As shown in Figure 6b, when HF waves at 6 MHz propagate through the plasma bubble of P2, that is, the RMS $\Delta N/N$ is 75%, there is relatively clear refraction on the radio waves. Compared with Figure 6a, the radio rays exhibit a more pronounced focusing effect, with a lower altitude of the focusing point. In addition, the radio rays reflected to the ground propagate a longer distance, and the single-hop distance can be up to 200 km.

The simulation results of OTHR shortwaves propagating through the EPB when the radio frequency is 8 and 10 MHz are shown in the following figure. From Figure 7, when the radio frequency increases to 8 and 10 MHz, all radio rays can penetrate the EPB and are no longer reflected to the ground. Radio waves exhibit the phenomenon of refraction when passing through the EPB and produce the focusing effect of electromagnetic waves. When OTHR waves propagate through the EPB of P2, that is, the RMS $\Delta N/N$ is 75%, the EPB has a greater influence on the radio waves than P1, and the radio rays are refracted to a greater degree. Moreover, the focusing effect of the rays is more obvious, and the height of the focusing point is lower. This is because when the RMS $\Delta N/N$ is larger, it indicates a large electron density gradient between the EPB and the background ionosphere. For the same transmission frequency, radio waves show a more significant focusing effect. Compared with 6 and 8 MHz shortwaves, the focusing effect of the 10 MHz radio waves diminishes, and the altitude of the focusing point increases accordingly. It can be concluded that the focusing effect of shortwaves will weaken gradually as the radio frequency increases, and the focusing point will rise gradually.

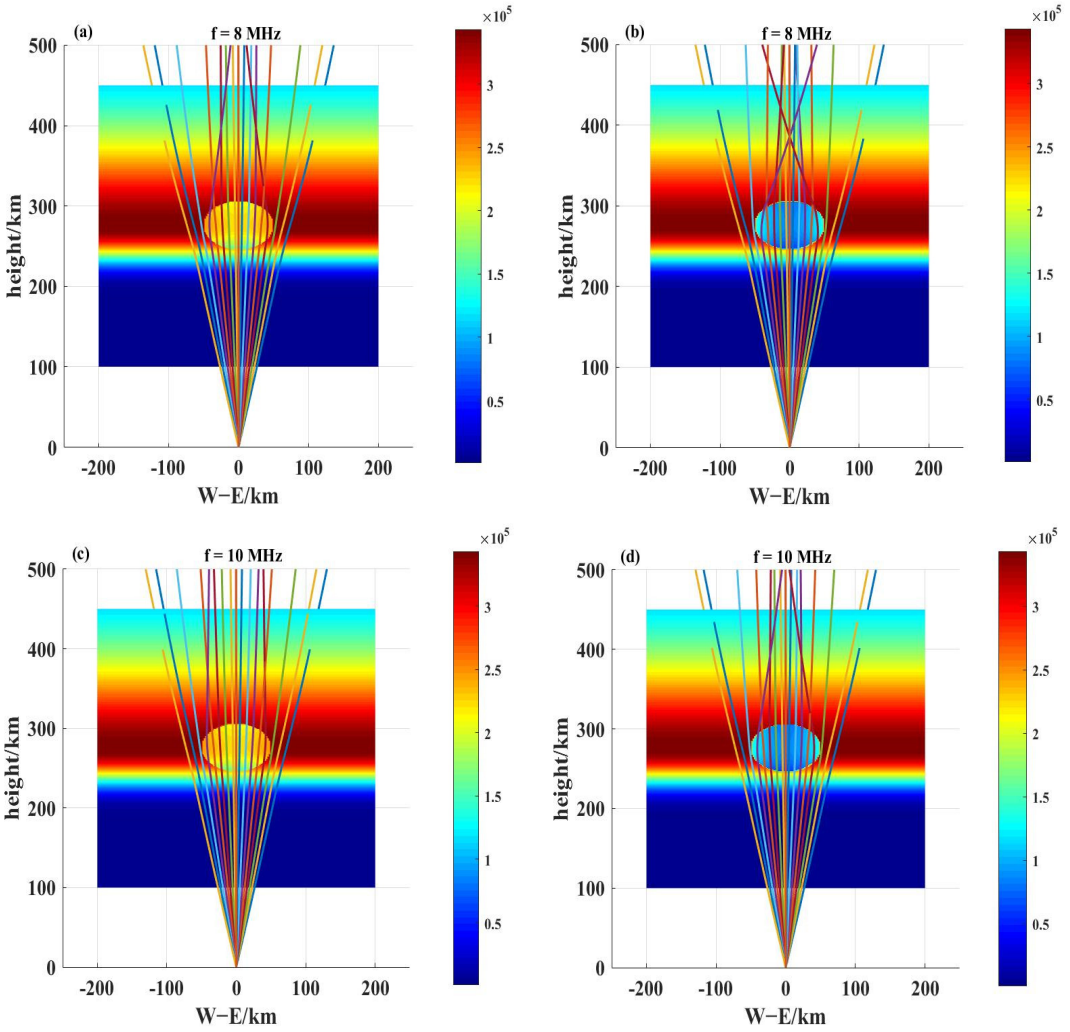

Figure 7. Simulation results of 8 and 10 MHz shortwaves propagating through EPBs. (**a**) Simulation results of 8 MHz waves propagating through EPB with RMS = 35%; (**b**) Simulation results of 8 MHz waves propagating through EPB with RMS = 75%; (**c**) Simulation results of 10 MHz waves propagating through EPB with RMS = 35%; (**d**) Simulation results of 10 MHz waves propagating through EPB with RMS = 75%.

Regarding the difference between the EPB model and real EPBs, we will further discuss their different impacts on radio wave propagation. When OTHR shortwaves propagate through real EPBs, their propagation path may be more complicated. As radio waves at various elevation angles encounter EPBs, there may be several different propagation modes. For example, some rays may be reflected, some rays may penetrate the EPB, and some rays may be reflected multiple times inside the EPB. Due to the presence of irregularities embedded in the EPB structure, in addition to reflection or refraction, the HF radio waves may be backscattered when encountering irregularities [25]. Since the density gradient at the EPB boundary may be larger, the refraction and focusing effects of radio waves may be more significant.

4.2. Simulation Results of OTHR Radio Waves for Different Seasons

Next, we simulated the propagation path of OTHR radio waves through EPBs in different seasons, namely, spring, summer, autumn, and winter. In this simulation, the EPB was set with the RMS $\Delta N/N$ of 75%, that is, the EPB is P2, and the time was set to 20LT at night on 15 March, 15 June, 15 September, and 15 December 2019, respectively, representing the simulation results of spring, summer, autumn, and winter. It was assumed that the

EPB appears at an altitude of 300 km, and the OTHR waves are transmitted in Haikou. The frequency of radio waves was set to 6 MHz, with an elevation angle range of 75–105°. Figure 8 shows the simulation results of shortwave propagation through the EPB in the four seasons.

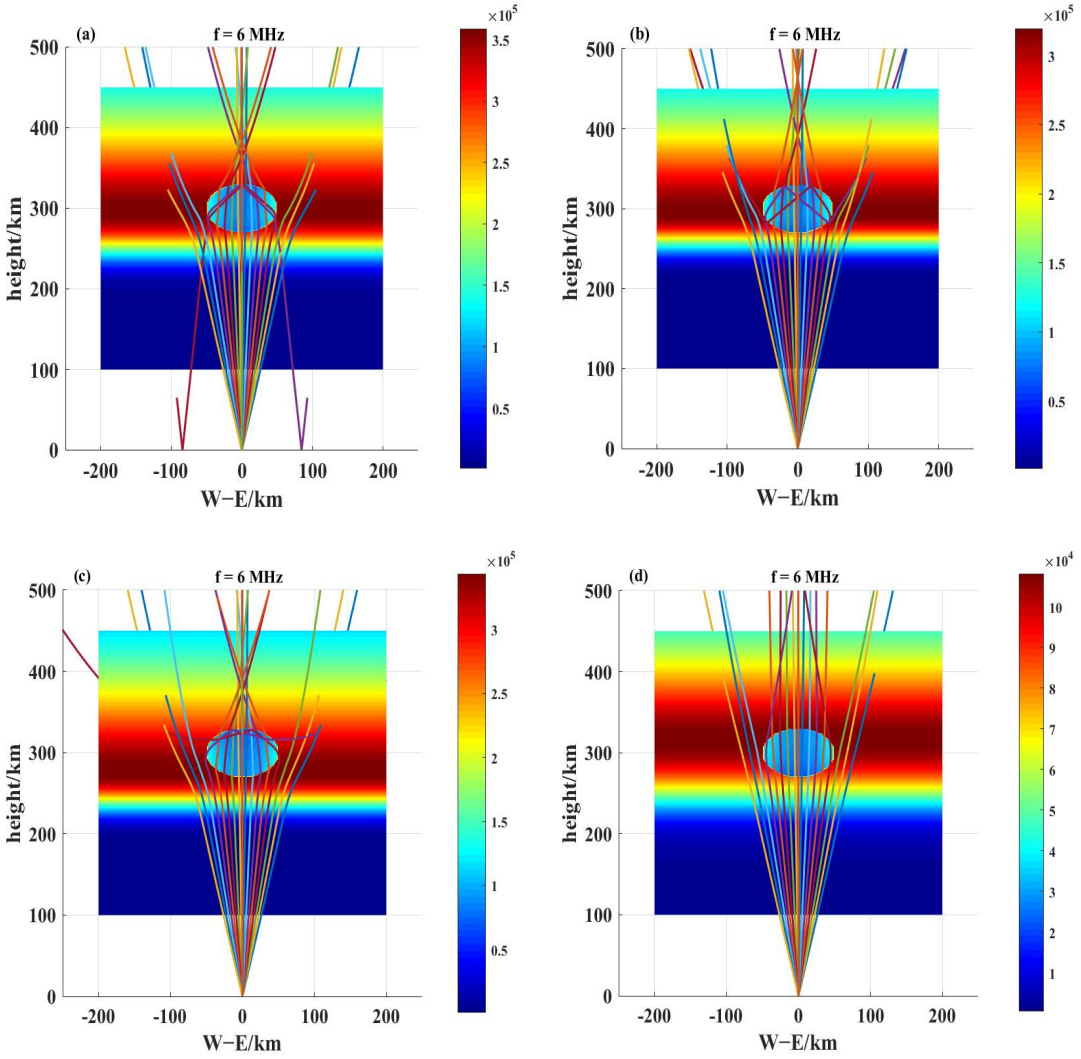

Figure 8. Simulation results of 6 MHz shortwaves propagating through EPB in four seasons. (**a**) Simulation results of 6 MHz waves in spring; (**b**) Simulation results of 6 MHz waves in summer; (**c**) Simulation results of 6 MHz waves in autumn; (**d**) Simulation results of 6 MHz waves in winter.

From Figure 8, the echo paths of 6 MHz HF waves through the EPB are different in the four seasons. In spring, as can be seen from Figure 8a, radio waves exhibit significant refraction as they propagate through the EPB, producing a pronounced focusing effect. Radio waves at 6 MHz exhibit a phenomenon of partial reflection and partial penetration. Some radio rays penetrate the lower boundary of the EPB, subsequently undergoing reflection at its upper boundary. The reason for this phenomenon is that the electron density at the upper boundary of the EPB is greater than that at the lower boundary, so the shortwaves can penetrate the lower layer but cannot penetrate the upper layer. In addition, radio rays with other elevations can completely pass through the ionosphere.

In the seasons of summer, autumn, and winter, all the radio waves penetrate the EPB region and are no longer reflected to the ground, as can be seen from Figure 8b–d. In summer and autumn, radio rays with lower elevation are reflected at the upper boundary of the EPB, then pass through the EPB area and propagate upward without being reflected to the ground.

For the four seasons, radio waves exhibit different degrees of refraction when propagating through the EPB, showing an inward-focusing phenomenon. The focusing effect is most pronounced in spring, followed by autumn, then summer, and the weakest in winter. This phenomenon can be attributed to the higher electron density in the background ionosphere in spring, reaching a maximum of about 3.5×10^5 el/cm^3, as shown in Figure 8a. Compared with other seasons, the gradient in electron density between the EPB and the background ionosphere is larger in spring, resulting in a more pronounced focusing effect when radio waves propagate through the EPB.

Figure 9 displays the 3D ray-tracing results of 6 MHz shortwaves in the four seasons. In spring, summer, autumn, and winter, there are significant differences in the propagation path of radio waves through the EPB. From Figure 9a, radio waves exhibit a phenomenon of partial penetration and partial reflection in spring; some of the rays propagating through the EPB are reflected to the ground, while other rays can penetrate the ionosphere. In other seasons, radio waves at all elevation angles pass through the ionosphere and are not reflected to the ground. Especially in winter, as shown in Figure 9d, the EPB has the least influence on the echo path of OTHR waves, the radio rays exhibit a relatively small degree of refraction and bending, and the focusing effect is the weakest.

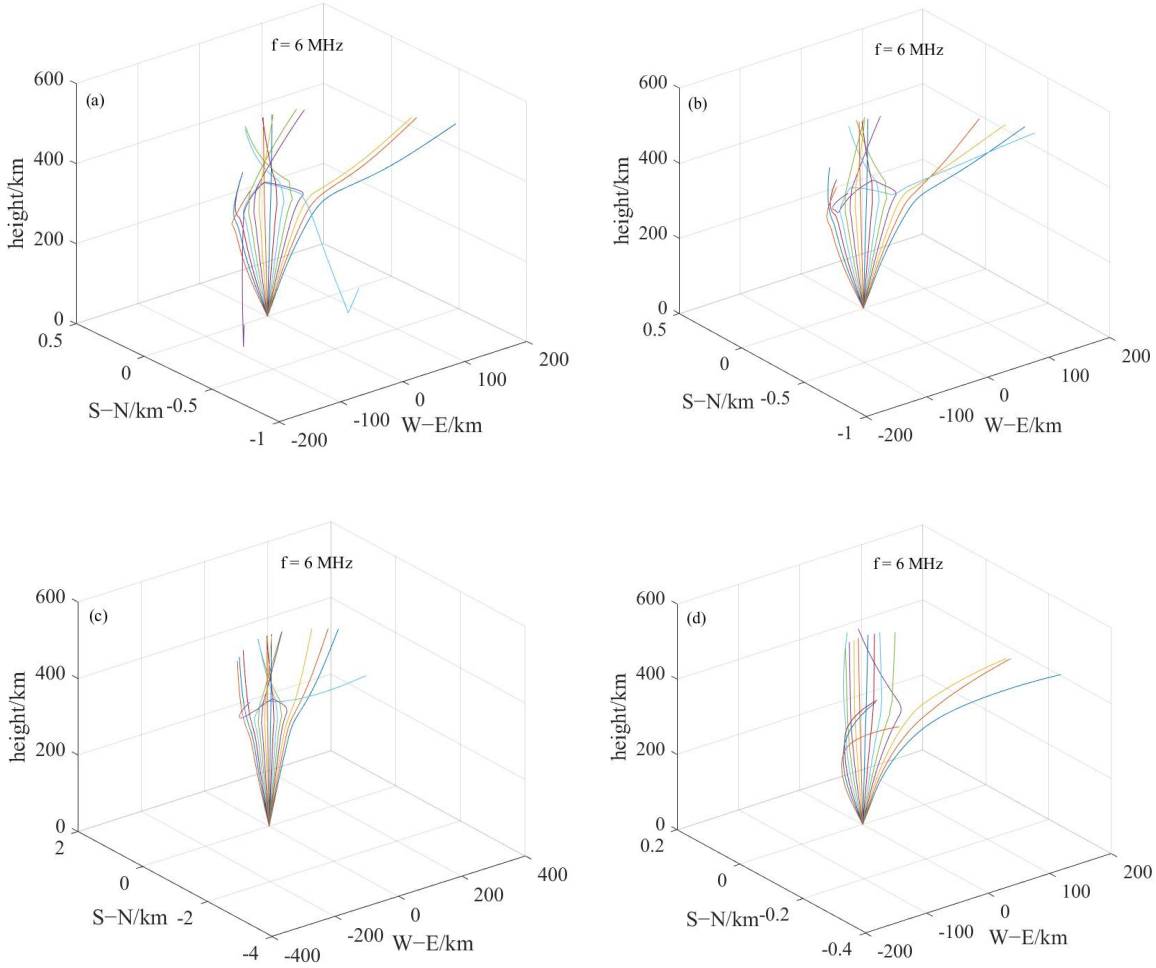

Figure 9. 3D ray-tracing results of 6 MHz shortwaves in four seasons. (**a**) 3D ray-tracing results of 6 MHz waves in spring; (**b**) 3D ray-tracing results of 6 MHz waves in summer; (**c**) 3D ray-tracing results of 6 MHz waves in autumn; (**d**) 3D ray-tracing results of 6 MHz waves in winter.

4.3. Simulation Results of OTHR Shortwaves for Different Solar Activities

The propagation path of OTHR shortwaves through the EPB was simulated and analyzed in different solar activity years. For the simulation, the time was set to 20:00 LT

on 15 September 2019 and 15 September 2014, representing the low- and high-solar-activity years, respectively. Assuming the frequencies of OTHR waves are 8, 12, and 15 MHz, respectively, the EPB occurs at an altitude of 300 km, with an RMS $\Delta N/N$ of 75% at the EPB center, and the elevation angle was set to 75–105°. Figure 10 shows the simulation results of OTHR shortwaves in the low- and high-solar-activity years.

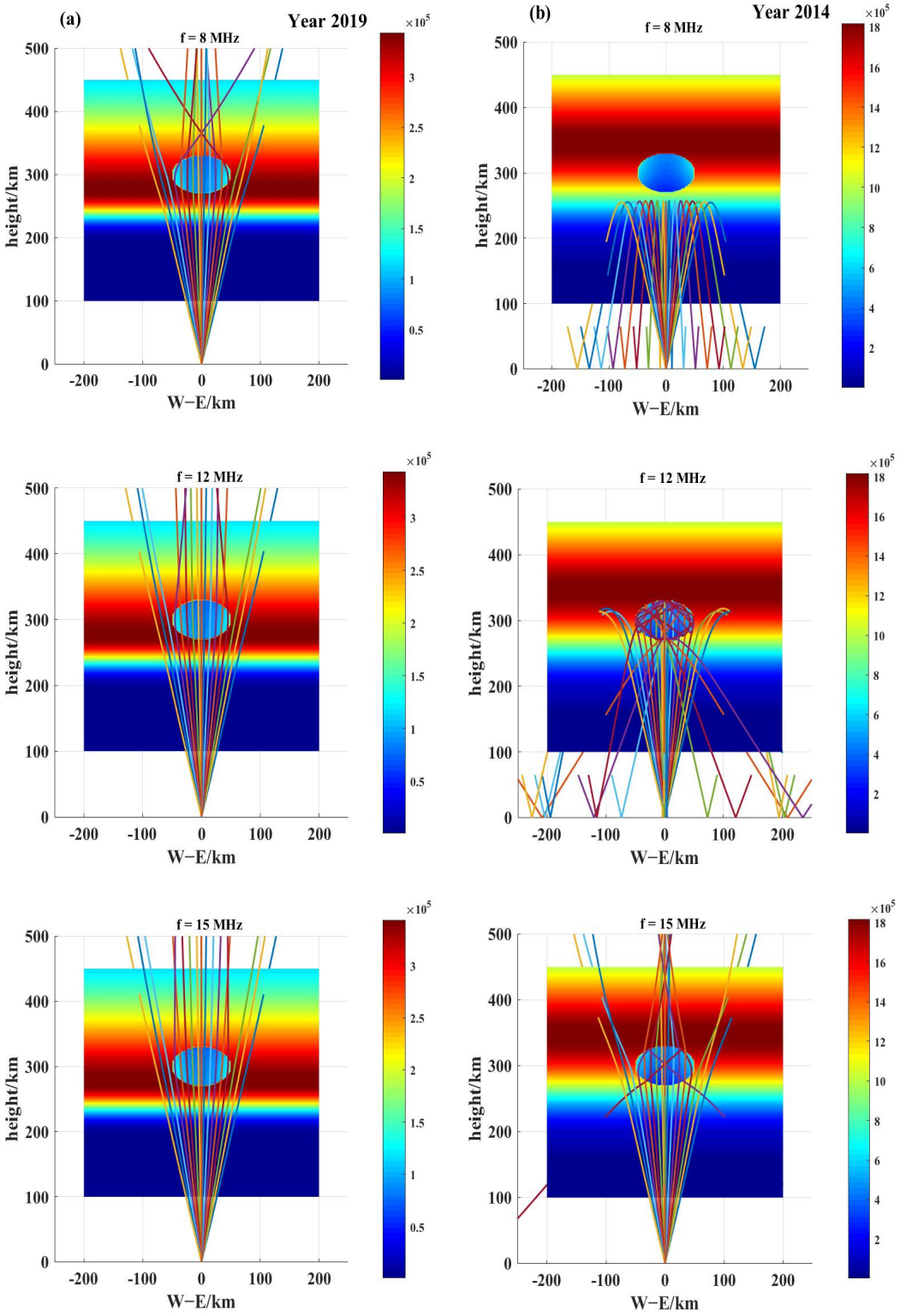

Figure 10. Simulation results of radio waves in the years 2019 and 2014. (**a**) Simulation results of HF waves in 2019; (**b**) Simulation results of HF waves in 2014.

Figure 10 presents the echo path of shortwaves at the frequencies of 8, 12, and 15 MHz. Figures 10a and 10b represent the simulation results of OTHR shortwaves in low- and high-solar-activity years, respectively. From Figure 10a, during the low-solar-activity year, when the radio frequencies are 8 MHz, 12 MHz, and 15 MHz, the radio waves entirely penetrate the ionosphere and are no longer reflected to the ground. When radio waves propagate through the EPB, the refraction and focusing effect occurs, and the focusing effect of 8 MHz waves is relatively significant. As the frequency increases, the focusing effect of the radio rays gradually weakens and the focusing point gradually increases. When the radio frequency increases to 15 MHz, the EPB has less influence on the radio waves, resulting in a weaker focusing effect.

In comparison, during the high-solar-activity year, the 8 MHz waves do not reach the height region of the EPB and are entirely reflected to the ground, with a reflection height of approximately 260 km. When the frequency of radio waves is 12 MHz, radio waves can pass through the lower boundary of the EPB, exhibiting a complex propagation path. In addition, radio rays propagating through the EPB are all reflected at its upper boundary, subsequently returning to the ground. When the radio frequency increases to 15 MHz, most of the radio rays penetrate the ionosphere, while some rays with lower elevation are reflected at the upper boundary of the EPB and finally reflected to the ground. The propagation type of 15 M shortwaves is partial penetration and partial reflection.

In conclusion, the impact of the EPB on radio waves in high solar activity is significantly greater than that in low solar activity. In the case of the same radio frequency, such as 15 MHz, during the high-solar-activity year, radio waves propagating through the EPB are refracted to a greater extent, the transmitted shortwaves exhibit a more significant focusing effect, and the altitude of the focusing point is relatively lower than in the low solar activity.

5. Conclusions

Plasma bubbles are the typical irregular structures that often appear in the F layer at night, which can affect the radio wave propagation of sky-wave radar, so it is of great significance to study the effect of plasma bubbles on OTHR detection. In this study, an ellipsoidal-shaped EPB model was built, and the density fluctuations in the east–west orientation follow the Gaussian function distribution. Based on the numerical 3D ray-tracing algorithm, the echo path of OTHR shortwaves propagating through EPBs can be simulated. The impact of EPBs with different RMS $\Delta N/N$ on OTHR shortwaves was analyzed and studied. Considering different seasons and solar activities, we simulated the echo path of OTHR radio waves propagating through EPBs. The simulation results in this study can serve as a reference for frequency selection in OTHR and HF communications, and can efficiently improve OTHR performance. Our main conclusions and findings are listed below:

(1) Based on the three-dimensional model of EPBs, the impact of EPBs with different RMS $\Delta N/N$ on OTHR waves was studied. The simulation results show that when 6 MHz shortwaves propagate through an EPB, the radio waves show partial penetration and partial reflection. Radio waves with lower elevation undergo reflection at the upper boundary of the plasma bubble, subsequently returning to the ground. Radio waves at 8 and 10 MHz exhibit the phenomenon of total penetration. As the frequency increases, the focusing effect of radio waves gradually diminishes, and the focusing point gradually increases. When OTHR waves propagate through EPBs with different RMS ΔN/N, their echo paths exhibit significant differences. When the RMS $\Delta N/N$ = 75%, radio waves demonstrate a more pronounced focusing effect than at lower RMS, with a lower altitude of the focusing point;

(2) When radio waves propagate through EPBs in different seasons, the influence of the EPB on OTHR shortwaves was analyzed and studied. The simulation results indicate that the propagation path of 6 MHz waves through EPB is completely different in the four seasons. In spring, radio waves propagating through EPB produce significant refraction, and the propagation type is partial penetration and partial reflection. In the

seasons of summer, autumn, and winter, all radio waves pass through the EPB area and propagate upward, showing the characteristics of total penetration. In addition, radio waves show an inward-focusing effect and have different degrees of refraction in the four seasons. The focusing effect is the most significant in spring, followed by autumn, then summer, and the weakest in winter. It can be concluded that the EPB has a greater impact on OTHR waves in spring;

(3) For different solar activities, the echo path of OTHR waves propagating through EPBs was simulated in the years 2019 and 2014. In the low-solar-activity year, all radio waves at 8, 12, and 15 MHz penetrate the ionosphere, showing the type of total penetration. In the year of high solar activity, the 8 MHz radio waves do not reach the EPB height area and are all reflected to the ground. When the radio frequency is 12 MHz, all radio waves propagating through the EPB are reflected at the upper boundary of the EPB and finally reflected to the ground. The 15 MHz waves exhibit partial penetration and partial reflection. For the same radio frequency, the impact of the EPB on the echo path of OTHR waves is greater in the high-solar-activity year, and the radio waves exhibit a clear refraction effect.

Author Contributions: Conceptualization, X.M. and P.G.; Investigation, X.M. and D.Y.; Methodology, M.W. and H.Y.; Writing—original draft preparation, X.M. and P.G.; Writing—review and editing, M.W. and D.Y. All authors have read and agreed to the published version of the manuscript.

Funding: This research was funded by the National Natural Science Foundation of China (grant numbers 12273093 and 12273094), the Natural Science Foundation of Shanghai (grant number 23ZR1473800), the Guangdong Basic and Applied Basic Research Foundation (2023A1515011323), and the China Scholarship Council (202208440223).

Data Availability Statement: IRI-2016 data can be obtained via "https://kauai.ccmc.gsfc.nasa.gov/instantrun/iri/", the data are accessed on 1 June 2023.

Acknowledgments: We are grateful to our colleagues and Shujie Chang for their kind support in this study.

Conflicts of Interest: The authors declare no conflicts of interest.

References

1. Booker, H.G.; Wells, H.W. Scattering of radio waves by the F-region of the ionosphere. *J. Geophys. Res. Atmos.* **1938**, *43*, 249–256. [CrossRef]
2. Kelley, M.C. *The Earth's Ionosphere: Plasma Physics and Electrodynamics*; Academic Press: San Diego, CA, USA, 1989.
3. Sultan, P.J. Linear theory and modeling of the Rayleigh-Taylor instability leading to the occurrence of equatorial spread F. *J. Geophys. Res. Space Phys.* **1996**, *101*, 26875–26891. [CrossRef]
4. Wu, Q.; Yu, T.; Lin, Z.X.; Xia, C.-L.; Zuo, X.-M.; Wang, X. Night airglow observations to irregularities in the ionospheric F region over Hainan Chinese. *J. Geophys.* **2016**, *59*, 17–27.
5. Ma, X.; Wu, M.; Guo, P.; Xu, J. Airglow Observation and Statistical Analysis of Plasma Bubbles over China. *Atmosphere* **2023**, *14*, 341. [CrossRef]
6. Sun, L.; Xu, J.; Wang, W.; Yuan, W.; Li, Q.; Jiang, C. A statistical analysis of equatorial plasma bubble structures based on an all-sky airglow imager network in China. *J. Geophys. Res. Space Phys.* **2016**, *121*, 11495–11517. [CrossRef]
7. Woodman, R.F.; Hoz, C.L. Radar observations of F region equatorial irregularities. *J. Geophys. Res.* **1976**, *81*, 5447–5466. [CrossRef]
8. Weber, E.J.; Buchau, J.; Eather, R.H.; Mende, S.B. North-south aligned equatorial airglow depletions. *J. Geophys. Res.* **1978**, *83*, 712–716. [CrossRef]
9. Makela, J.J. A review of imaging low-latitude ionospheric irregularity processes. *J. Atmos. Sol.-Terr. Phys.* **2006**, *68*, 1441–1458. [CrossRef]
10. Ma, X.; Guo, P.; Wu, M. Simulation research on the influence of plasma bubbles on radio wave propagation. *Radio Sci.* **2023**, *58*, e2022RS007577. [CrossRef]
11. Chen, G.; Zhao, Z.; Zhang, Y. Ionospheric Doppler and echo phase measured by the Wuhan Ionospheric Oblique Backscattering Sounding System. *Radio Sci.* **2007**, *42*, RS4007. [CrossRef]
12. Chen, G.; Zhao, Z.; Li, S.; Shi, S. WIOBSS: The Chinese low-power digital ionosonde for ionospheric backscattering detection. *Adv. Space Res.* **2009**, *43*, 1343–1348. [CrossRef]
13. Han, Y.M.; Xiong, J.Q.; Lou, P. A Study on the Impact of Ionospheric Es Layer on the Over-the-horizon Radar Performance. *Chin. Mod. Radar* **2017**, *39*, 14–17.

14. Carrano, C.S.; Groves, K.M.; Caton, R.G.; Rino, C.L.; Straus, P.R. Multiple phase screen modeling of ionospheric scintillation along radio occultation raypaths. *Radio Sci.* **2011**, *46*, RS0D07. [CrossRef]
15. Thayaparan, T.; Warrington, M.; Stocker, A.; Siddle, D. Effect of Frequency Monitoring System for Over-The-Horizon Radar due to the presence of patches and arcs within the polar cap ionosphere. In Proceedings of the 2020 21st International Radar Symposium (IRS), Warsaw, Poland, 5–8 October 2020.
16. Zhao, H.S.; Xu, Z.W.; Wang, Y.W.; Xie, S.-Z.; Xue, K.; Wang, C.; Wu, J.; Gao, J.-F.; Xu, Z.-H.; Zheng, Y.-S. Over-the-Horizon Channel of Radio Communication at VHF Band via Artificial Plasma Clouds. *IEEE Trans. Antennas Propag.* **2022**, *70*, 5795–5803. [CrossRef]
17. Zhao, H.S.; Xu, Z.W.; Tang, W.; Xu, Z.-H.; Xue, K.; Xie, S.-Z.; Zheng, Y.-S.; Wu, J.; Zhang, J.-D. Electromagnetic Scattering by Artificial Plasma Clouds in the Ionosphere. *IEEE Trans. Antennas Propag.* **2020**, *68*, 4810–4819. [CrossRef]
18. Ma, X.; Fang, H.; Wang, S.; Chang, S. Impact of the Ionosphere Disturbed by Rocket Plume on OTHR Radio Wave Propagation. *Radio Sci.* **2021**, *56*, e2020RS007183. [CrossRef]
19. Chen, S.-P.; Lin, C.H.; Rajesh, P.K.; Liu, J.-Y.; Eastes, R.; Chou, M.-Y.; Choi, J.-M. Near real-time global plasma irregularity monitoring by FORMOSAT-7/COSMIC-2. *J. Geophys. Res. Space Phys.* **2021**, *126*, e2020JA028339. [CrossRef]
20. Zaalov, N.Y.; Moskaleva, E.V. Oblique and vertical incidence ionogram simulations with the presence of Es layer. *Adv. Space Res.* **2020**, *66*, 1713–1723. [CrossRef]
21. Hu, Y.G.; Zhao, Z.Y.; Zhang, Y.N. Ionospheric disturbances produced by chemical releases and the resultant effects on short-wave ionospheric propagation. *J. Geophys. Res.* **2011**, *116*, A07307. [CrossRef]
22. Ma, X.; Fang, H. Optical observation of plasma bubbles and comparative study of multiple methods of observing the ionosphere over China. *Adv. Space Res.* **2020**, *65*, 2761–2772. [CrossRef]
23. Wernik, A.W.; Alfonsi, L.; Materassi, M. Scintillation modeling using in situ data. *Radio Sci.* **2007**, *42*, RS1002. [CrossRef]
24. Wang, G.J.; Shi, J.K.; Cheng, Z.W.; Wang, X.; Wang, Z. Ionospheric plasma bubbles simultaneously observed by multi-instruments in Hainan region. *Chin. J. Radio Sci.* **2014**, *29*, 66–71.
25. Hu, L.; Li, G.; Ning, B.; Sun, W.; Xie, H.; Zhao, X.; Li, Y.; Dai, G.; Xiao, Q.; Yan, Y. Development of low latitude long range ionospheric radar for observing plasma bubble irregularities and preliminary results. *J. Geophys. Res. Space Phys.* **2024**, *129*, e2023JA032099. [CrossRef]